$\mathcal{H}_\infty$ Control Design for a Magnetostrictive Transducer

James Nealis and Ralph C. Smith

Center for Research in Scientific Computation, North Carolina State University, Raleigh, NC 27695

Abstract

Magnetostrictive transducers are becoming increasingly prevalent in industrial applications including high speed milling and hybrid motor design due to their broadband, large force capabilities. To achieve the level of performance required by such applications, however, these transducers must operate in nonlinear and hysteretic regimes. To accommodate this nonlinear behavior, models and control laws must incorporate known physics and be sufficiently robust to operate under realistic operating conditions. We develop here an $\mathcal{H}_\infty$ robust control design for a prototypical magnetostrictive transducer but note that the design is sufficiently general to be utilized for several commonly used smart materials including piezoceramics and shape memory alloys. The performance of the control strategy is illustrated through a numerical example.

1. Introduction

Applications utilizing piezoceramic (PZT), magnetostrictive and shape memory alloy (SMA) compounds range from nanopositioning stages in an atomic force microscope (AFM) to vibration suppression systems in buildings. However, the material attributes which provide these compounds with unique control capabilities also produce hysteresis and constitutive nonlinearities which must be accommodated in models and control algorithms to meet the stringent design criteria associated with these applications.

The method we employ to attenuate this nonlinear and hysteretic behavior is to utilize an approximate inverse of the hysteresis model as a filter to mitigate these effects. This control strategy requires a hysteresis model which admits an inverse that can be employed in real-time. Filters of this type have been constructed using a domain wall model [6, 8] as well as Preisach models [12]. Here we utilize a free-energy based hysteresis model [9] and a corresponding approximate inverse algorithm which lends itself to real-time implementation.

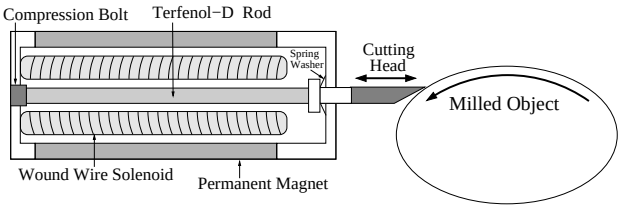

Figure 1. Terfenol-D transducer.

To focus the discussion, we consider an industrial application requiring high speed, high accuracy milling using the prototypical magnetostrictive actuator illustrated in Figure 1. The objective of this application is milling out-of-round objects at speeds of 3000 rpm within a tolerances of 1-2 microns. Stresses and displacements are provided by the Terfenol-D rod in response to applied fields generated by the surrounding solenoid. A permanent magnet encasing the transducer provides a biased field to achieve bidirectional strains as well as providing a mechanism for flux shaping.

As detailed in [1, 2], these transducers possess the ability to generate broadband, high force responses. However, they also exhibit hysteresis and nonlinearities in the relation between the input field H and the magnetization M generated in the Terfenol-D rod. We focus on this magnetostrictive transducer in this paper but note that the hysteresis model and control design are sufficiently general to permit direct extension to analogous piezoelectric and shape memory alloy models as developed in [3, 10, 11].

Whereas employing an inverse filter attenuates the primary effects of the nonlinear and hysteretic behavior of the smart materials, there are still disturbances in the process due to discretization and modeling errors as denoted by d in Figure 2. In realistic applications, the errors d are not the only disturbance to the control system which must be accommodated. Sensor noise is also present in all applications and can cause a degradation in the transducer performance if unaccommodated. Therefore, we consider an $\mathcal{H}_\infty$ design capable of rejecting both classes of disturbances.

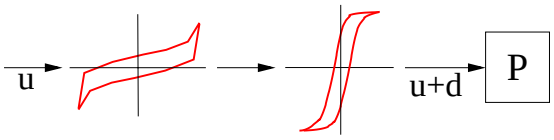

Figure 2. Approximate model inverse employed as a filter for robust control design.

2. Hysteresis Model

We summarize here the relevant aspects of the hysteresis model presented in [9]. This model quantifies the energy required to reorient moments in combina-

Report Documentation Page

Form Approved
OMB No. 0704-0188

1. REPORT DATE	2. REPORT TYPE	3. DATES COVERED
2003		**00-00-2003 to 00-00-2003**

4. TITLE AND SUBTITLE	5a. CONTRACT NUMBER
H1 Control Design for a Magnetostrictive Transducer	5b. GRANT NUMBER
	5c. PROGRAM ELEMENT NUMBER
6. AUTHOR(S)	5d. PROJECT NUMBER
	5e. TASK NUMBER
	5f. WORK UNIT NUMBER
7. PERFORMING ORGANIZATION NAME(S) AND ADDRESS(ES) **North Carolina State University,Center for Research in Scientific Computation,Raleigh,NC,27695-8205**	8. PERFORMING ORGANIZATION REPORT NUMBER
9. SPONSORING/MONITORING AGENCY NAME(S) AND ADDRESS(ES)	10. SPONSOR/MONITOR'S ACRONYM(S)
	11. SPONSOR/MONITOR'S REPORT NUMBER(S)

12. DISTRIBUTION/AVAILABILITY STATEMENT
Approved for public release; distribution unlimited

13. SUPPLEMENTARY NOTES
The original document contains color images.

14. ABSTRACT
see report

15. SUBJECT TERMS

16. SECURITY CLASSIFICATION OF:			17. LIMITATION OF ABSTRACT	18. NUMBER OF PAGES	19a. NAME OF RESPONSIBLE PERSON
a. REPORT	b. ABSTRACT	c. THIS PAGE			
unclassified	**unclassified**	**unclassified**		**6**	

tion with stochastic homogenization techniques to accommodate variations in coercive and effective fields. We assume fixed temperatures for this development and the model ignores losses due to eddy currents and therefore should be employed for operating regimes in which eddy current losses are negligible. A further assumption is that the spring washer in the transducer provides sufficient prestress to dominate crystalline anisotropies.

We first quantify the internal energy due to the interaction of moments through the Helmholtz energy. As detailed in [9], under the assumption that moments orient either with the applied field or diametrically opposite to it, a reasonable form of the Helmholtz energy is

$$\psi = \begin{cases} \frac{\eta}{2}(M+M_R)^2 & , M \le -M_I \\ \frac{\eta}{2}(M-M_R)^2 & , M \ge M_I \\ \frac{\eta}{2}(M_I - M_R)\left(\frac{M^2}{M_I} - M_R\right) & , |M| < M_I. \end{cases} \quad (1)$$

As depicted in Figure 3, M_R and M_I respectively denote the point at which the minimum of ψ occurs and the inflection point.

In the presence of an applied field H, the Gibbs energy is given by

$$\mathcal{G} = \psi(M) - HM. \quad (2)$$

We note the magnetostatic energy is $\mathcal{E} = \mu_0 HM$, where μ_0 denotes the magnetic permeability, so the Gibbs relation (2) can be interpreted as incorporating μ_0 into ψ.

Magnetoelastic coupling can be incorporated through the extended Helmholtz relation

$$\psi_e(M,\varepsilon) = \psi(M) + \frac{1}{2}Y^M\varepsilon^2 - Y^M\gamma\varepsilon M^2$$

and the corresponding Gibbs energy

$$G(H,M,\varepsilon) = \psi(M) + \frac{1}{2}Y^M\varepsilon^2 - Y^M\gamma\varepsilon M^2 - HM - \sigma\varepsilon.$$

Here, ψ is specified by (1), Y^M is the Young's modulus at constant magnetization, γ is a magnetoelastic coupling coefficient, σ is the applied stress and ε denotes the strains.

For operating regimes in which thermally activated processes are negligible, the local average magnetization can be quantified from the necessary condition $\frac{\partial \mathcal{G}}{\partial M} = 0$. In the absence of applied stresses, the local model thus predicts a linear relationship between H and $\overline{M}$ with slope $\frac{1}{\eta}$. As detailed in [9], the local magnetization in this limiting case is given by

$$[\overline{M}(H,;H_c,\xi)](t) = \begin{cases} [\overline{M}(H;H_c,\xi)](0) \\ \frac{H}{\eta} - M_R \\ \frac{H}{\eta} + M_R \end{cases} \quad (3)$$

for the respective cases $\{\tau(t) = \emptyset\}$, $\{\tau(t) \neq \emptyset$ and $H(\max\tau(t)) = -H_c\}$, $\{\tau(t) \neq \emptyset$ and $H(\max\tau(t)) = H_c\}$. The transition points are specified as

$$\tau(t) = \{t \in (0,T_f] \mid H(t) = -H_c \text{ or } H(t) = H_c\}$$

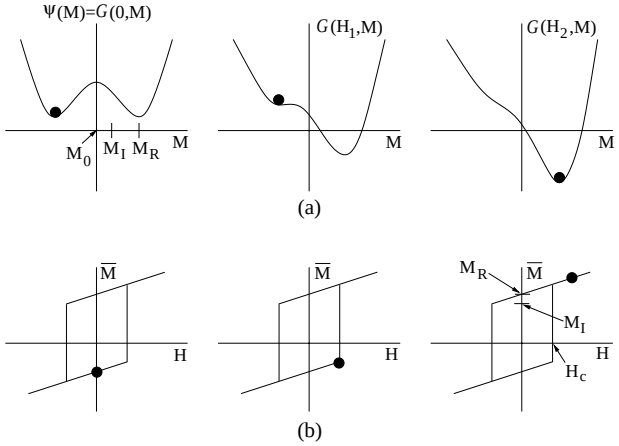

Figure 3. (a) Helmholtz energy ψ and Gibbs energy $\mathcal{G}$ for increasing fields H. (b) Dependence of the local magnetization $\overline{M}$ on the field H at the lattice level in the absence of thermal activation.

and the initial moment orientation is

$$[\overline{M}(H;H_c,\xi)](0) = \begin{cases} \frac{H}{\eta} - M_R \ , H(0) \le -H_c \\ \xi \quad , -H_c < H(0) < H_c \\ \frac{H}{\eta} + M_R \ , H(0) \ge H_c \ . \end{cases}$$

For a description of models which incorporate thermal activation, the reader is referred to [9].

The relation (3) is derived under the assumption that the lattice structure is homogeneous which is overly simplistic in that it neglects material defects, polycrystallinity and material nonuniformities. Also, the model assumes that the effective field H_e at the domain level is the applied field H. To incorporate these effects, stochastic distributions are employed to develop a bulk magnetization model for nonhomogeneous Terfenol-D samples with nonconstant effective fields (see [9] for details).

To include the effects of material nonhomogeneities, we consider a distribution of free energy profiles to accommodate the nonhomogeneous lattice structures. We assume that the local coercive field $H_c = \eta(M_R - M_I)$ is normally distributed with mean $\overline{H}_c$. Hence the coercive field has the density

$$f(H_c) = C_1 e^{-(H_c - \overline{H}_c)^2/b}$$

where the parameters C_1 and b are positive.

The second extension entails the incorporation of variations in the effective field through the assumption that it is normally distributed about the applied field H. Therefore, the effective field has the density

$$\widehat{f}(H_e) = C_2 e^{-(H-H_e)^2/\overline{b}}$$

where C_2 and $\overline{b}$ are positive. Combination of the coercive and effective field distributions yields the magne-

tization relation

$$M(H) = C \int_0^\infty \int_{-\infty}^\infty [\overline{M}(H; H_c, \xi)] f(H_c) \widehat{f}(H_e) dH_e dH_c. \tag{4}$$

The integrals are approximated using a composite quadrature rule for the numerical implementation of the free energy model thus allowing the hysteresis model to be computed algebraically and hence at low cost. Because of the exponential decay of the distributions, they can be truncated to speed computation. The model is thus sufficiently efficient to allow the possibility of real time implementation.

The elastic constitutive relation is provided by the equilibrium condition $\frac{\partial G}{\partial \varepsilon} = 0$ which yields

$$\sigma = Y^M \varepsilon - Y^M \gamma M^2. \tag{5}$$

The coupled constitutive relations (4) and (5) quantify the magnetization and stresses for an undamped magnetostrictive material. These relations are employed in Section 4 when quantifying the displacements produced by the magnetostrictive transducer depicted in Figure 1.

3. Inverse Hysteresis Model

The monotonicity and efficiency of the hysteresis model are exploited to construct an approximate inverse. To determine the applied field required to create a desired magnetization, the hysteresis model is used to increment the magnetization until the desired magnetization is surpassed. Then the applied field is computed by linear interpolation. The computational speed of the inverse compensator depends on the size of the step ΔH taken in advancing the hysteresis model. Larger steps will increase the speed while decreasing the accuracy of the inverse compensator. The relative linearization error for an input signal with a frequency of 1 Hz and a step size of $\Delta H = 1$ employed in the inverse model is plotted in Figure 4. A successful control design must be able to reject this error to the input of the plant.

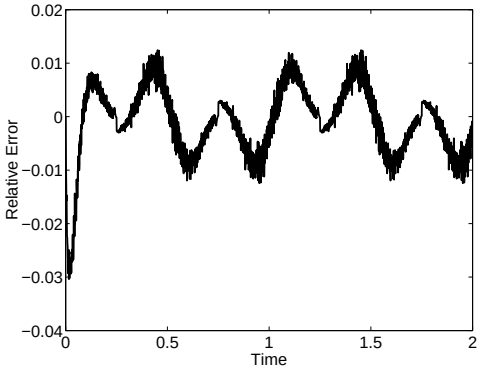

Figure 4. Relative error created by inverse filtering.

4. Transducer Model

In this section, we employ the relations (4) and (5) to quantify the displacements generated by applied fields in the prototypical transducer depicted in Figure 1. The model for the transducer is based on the model developed in [2].

One end of the rod ($x = 0$) is assumed to be fixed while the other end ($x = L$) is constrained by a damped oscillator and has an attached point mass as depicted in Figure 5. The internal damping coefficient and density of the Terfenol-D rod are denoted by c^M and ρ and the point mass is denoted M_L. The end spring has stiffness k_L and damping coefficient c_L.

The constitutive relation (5) is for an undamped material. To incorporate Kevin-Voigt damping, the stresses at any point x, $0 \le x \le L$, are assumed to be proportional to a linear combination of strain, strain rate and squared magnetization which yields

$$\sigma = Y^M \frac{\partial w}{\partial x} + c^M \frac{\partial^2 w}{\partial x \partial t} - Y^M \gamma M^2$$

where the linear strain relation $\varepsilon = \frac{\partial w}{\partial x}$ is employed.

Balancing forces yields

$$\rho A \frac{\partial^2 w}{\partial t^2} = \frac{\partial N_{tot}}{\partial x} \tag{6}$$

where A is the cross sectional area of the Terfenol-D rod and the force resultant $N_{tot} = \int_A \sigma dA$ is given by

$$N_{tot} = Y^M A \frac{\partial w}{\partial w} + c^M A \frac{\partial^2 w}{\partial x \partial t} - Y^M A \gamma M^2.$$

To obtain appropriate boundary conditions, we first note that $w(t, 0) = 0$. As detailed in [2], balancing forces at $x = L$ gives

$$N_{tot}(t, L) = -k_L w(t, L) - c_L \frac{\partial w}{\partial t}(t, L) - M_L \frac{\partial^2 w}{\partial t \partial t}(t, L).$$

Initial conditions are taken to be $w(0, x) = 0$ and $\frac{\partial w}{\partial t}(0, x) = 0$.

The model can be implemented utilizing the weak form and a Galerkin finite element approximation. To further simplify our system, we assert that the magnetization in the Terfenol-D rod can be taken as uniform

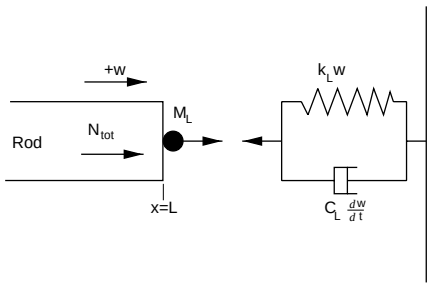

Figure 5. Boundary conditions for the rod model.

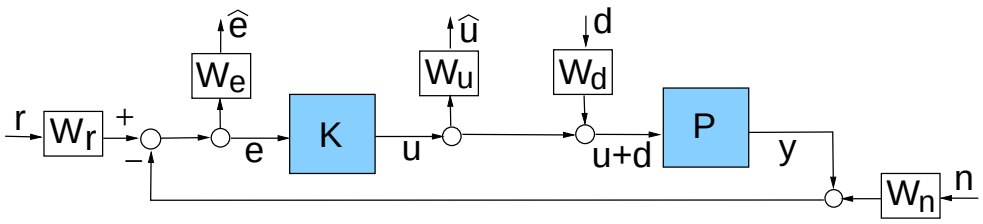

Figure 6. System representation including input disturbances d and sensor noise n.

over the length of the rod. This is reasonable in present actuator designs since flux shaping via the surrounding magnet is used to minimize end effects in the rod. Hence, since each section of the rod reacts identically to the uniform magnetic field, the elements act uniformly and therefore the transducer dynamics can be modeled as a damped spring-mass. To achieve bidirectional strains, we linearize the magnetostrictive relationship about a biasing magnetization level of $M_s/2$. This bias can be achieved my means of the permanent magnet as depicted in Figure 1. For more details on this model development see [2, 5].

The dynamics of the Terfenol-D transducer can be now represented by

$$\begin{aligned} \ddot{x} + k\dot{x} + cx &= \nu M(t) \\ x(0) = x_0 \quad , \quad \dot{x}(0) &= \dot{x}_0. \end{aligned} \tag{7}$$

The scalars k, c, and ν are determined by fitting the model (7) to the Galerkin approximation of (6) or to data from the physical device. For our sample, $k = 7.8899 \times 10^3$, $c = 6.4251 \times 10^7$ and $\nu = 1.3724 \times 10^{-2}$ yielded accurate model fits. Note that the hysteresis inherent to the Terfenol-D rod is still present in (7) through (4) which quantifies the hysteretic relationship between H and M.

5. Robust Control Design

In this section, we present a robust control design for the Terfenol-D transducer depicted in Figure 1. The control system incorporates the presence of external disturbances, such as the errors cause by the inverse filter and sensor noise, and minimizes their effects with respect to the $\mathcal{H}_\infty$ norm

$$\|T\|_\infty = \sup_{\omega \in \mathbb{R}} \overline{\sigma}[T(j\omega)]$$

where $\overline{\sigma}[T(j\omega)]$ denotes the maximum singular values of the closed-loop map T. Analogous $\mathcal{H}_2$ control laws are developed in [5, 7].

Figure 6 illustrates the block diagram of the system to be controlled. In the diagram, P represents the transducer model given by the differential equation (7). The signal to be tracked and the position of the tip of the Terfenol-D rod are respectively denoted by r and y. The signal d represents the error in the linearization of the input by the inverse filter (see Figure 4). The signal n represents noise in the sensor the measurements of y. For the simulation results presented in Section 6, we assume sensor noise with a frequency of 60 Hz. The output signals $\widehat{e}$ and $\widehat{u}$ denote the weighted tracking error and weighted output of the controller K, respectively. The weighting functions W_u, W_d, W_e, W_r and W_n are chosen to maximize the performance of the controller utilizing *a priori* knowledge regarding the characteristics of the signals.

We now construct the transfer function representation of the open-loop system. The transfer matrix from the inputs r, d, n and u to the outputs $\widehat{e}$, $\widehat{u}$ and v is specified by

$$G = \begin{bmatrix} W_e W_r & -W_e P W_d & -W_e W_n & -W_e P \\ 0 & 0 & 0 & W_u \\ W r & -P W_d & -W_n & -P \end{bmatrix}.$$

The control system can then be represented as a linear fractional transformation as shown in Figure 7. Details regarding the system formulation can be found in [5, 7].

To proceed, we partition G as

$$G(s) = \left[\begin{array}{c|cc} A & B_1 & B_2 \\ \hline C_1 & 0 & D_{12} \\ C_2 & D_{21} & 0 \end{array}\right] \tag{8}$$

where

$$\begin{aligned} G_{11} &= \left[\begin{array}{c|c} A & B_1 \\ \hline C_1 & 0 \end{array}\right], \quad G_{12} = \left[\begin{array}{c|c} A & B_2 \\ \hline C_1 & D_{12} \end{array}\right], \\ G_{21} &= \left[\begin{array}{c|c} A & B_1 \\ \hline C_2 & D_{21} \end{array}\right], \quad G_{22} = \left[\begin{array}{c|c} A & B_2 \\ \hline C_2 & 0 \end{array}\right], \end{aligned} \tag{9}$$

respectively represent the transfer functions from w to z, u to z, w to v, and u to v, (see Figure 7). To ensure the existence of a H_∞ sub-optimal controller, the following assumptions are made regarding the system:

1. $(A,\, B_1)$ is controllable and $(C_1,\, A)$ is observable,
2. $(A,\, B_2)$ is stabilizable and $(C_2,\, A)$ is detectable,
3. $D_{12}^* D_{12} > 0$ and $D_{21} D_{21}^* > 0$,
4. $\begin{bmatrix} A - j\omega I & B_2 \\ C_1 & D_{12} \end{bmatrix}$ has full column rank for all ω,

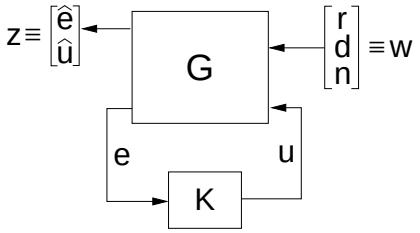

Figure 7. Linear fractional transformation (LFT) representation of transducer.

5. $\begin{bmatrix} A - j\omega I & B_1 \\ C_2 & D_{21} \end{bmatrix}$ has full row rank for all ω.

Details regarding the validity of these assumptions are provided in [5, 7].

5.1. Weighting Functions

The selection of the weighting functions is critical to the performance of the robust control design. A discussion of the choice of these function can be found in [4, 5, 7, 13]. By design, the frequency of the reference signal r is taken to be 1 Hz so we construct the pass-band filter W_r to have a bandwidth of 1 Hz centered at 1 Hz. The frequency of the noise n can be accurately determined for the device measuring the position of the tip of the Terfenol-D rod. For the simulation results, noise with a frequency of 60 Hz is added to the system so W_n is taken to be a pass-band filter with a bandwidth of 10 Hz centered at 60 Hz.

To determine the weighting function W_d, a signal with the same frequency as the reference signal was filtered by the inverse compensator and then fed into the hysteresis model. The output is defined to be the desired control signal plus the disturbance d (see Figure 2). The power spectrum of d indicates that the most significant frequencies in d lie below 400 Hz so W_d is taken as a low-pass filter with a cut-off frequency of 400 Hz.

The weighting function on the error signal was taken to be $W_e = \frac{\gamma_e}{s+\epsilon_e}$ with $\gamma_e = 4 \times 10^6$ and $\epsilon_e = 1 \times 10^{-8}$. An integrator was chosen to prevent the error from achieving steady state at a nonzero value and the pole was shifted slightly off zero to ensure that the controller design is realizable. We specified the weight on the controller output to be $W_u = 5 \times 10^{-6}$. Since we do not experience any problems with saturation or other such effects, we minimally weight $\widehat{u}$ to focus the controller on tracking and disturbance rejection. It is important to note that increasing the order of the filters increases the number of states in the controller design. To facilitate real-time implementation, a minimal control realization was utilized to limit the number of states in the control gain K.

5.2. $\mathcal{H}_\infty$ Sub-Optimal Control Design

Employing the notation defined in (9), the design of a sub-optimal $\mathcal{H}_\infty$ controller which gives $\|T\|_\infty < \gamma$ incorporates two Riccati equations

$$A^*X + XA + X\left(\gamma^{-2}B_1B_1^* - B_2B_2^*\right)X + C_1^*C_1 = 0 \tag{10}$$

and

$$AY + YA^* + Y\left(\gamma^{-2}C_1^*C_1 - C_2^*C_2\right)Y + B_1B_1^* = 0. \tag{11}$$

The following theorem from [13] guarantees the existence of an $\mathcal{H}_\infty$ sub-optimal control.

Theorem 1: There exists an admissible controller such that $\|T\|_\infty < \gamma$ if and only if

1. There exists a positive definite solution X to (10),
2. There exists a positive definite solution Y to (11),
3. $\rho(XY) < \gamma^2$.

The $\mathcal{H}_\infty$ optimal controller is subsequently given by

$$K \equiv \left[\begin{array}{c|c} A & -ZL \\ \hline F & 0 \end{array}\right] \tag{12}$$

with

$$A \equiv A + \gamma^{-2}B_1B_1^*X + B_2F + ZLC_2,$$
$$F \equiv -B_2^*X, \qquad L \equiv -YC_2^*.$$

The control given in (12) is sub-optimal in that it provides a closed-loop system with an $\mathcal{H}_\infty$-norm less than γ. The *hinfsyn* command in *Matlab* can be utilized to decrease γ until an assumption of Theorem 1 is violated. This yields a control design method which is close to optimal.

5.3. Numerical Example

We present here a numerical example illustrating the $\mathcal{H}_\infty$ robust control law. The results were computed using a noise signal n with a magnitude of 1×10^{-5}, which is 10% of the reference signal, and a frequency of 60 Hz. The inverse compensator was computed using a step size of $\Delta H = 1$ in the approximate inverse model to ensure a simulation of the control process which has the potential for real-time implementation. Figure 8a illustrates the controller's ability to track the reference signal and reject the noise and disturbance signals. A tracking error less that 2 microns is achieved after a short period, as illustrated in Figure 8b. Additional examples illustrating the performance of the method are provided in [7].

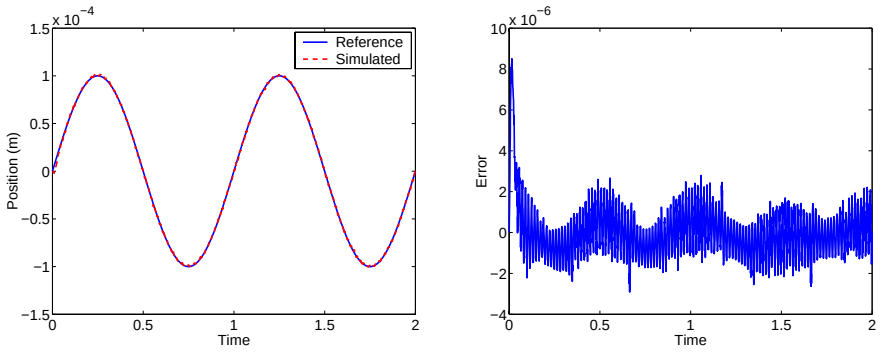

(a) (b)

Figure 8. (a) $\mathcal{H}_\infty$ tracking performance and (b) tracking error.

6. Concluding Remarks

An $\mathcal{H}_\infty$ robust control design for a magnetostrictive system has been summarized in this paper. It is shown that the $\mathcal{H}_\infty$ control design is capable of maintaining accurate tracking while rejecting sensor noise and a disturbance due to an inexact inverse filter. The same methodology can be used to include other disturbances to the system if necessary. Finally, while the methods were illustrated in the context of a magnetostrictive transducer, they are sufficiently general to be applied to systems utilizing piezoceramic or shape memory alloys due to the unified modeling framework used to quantify hysteresis and constitutive nonlinearities inherent to all of these materials [10].

Acknowledgments

This research was supported in part by the Air Force Office of Scientific Research under the grant AFOSR-F49620-01-1-0107.

References

[1] F.T. Calkins, R.C. Smith and A.B. Flatau, "An energy-based hysteresis model for magnetostrictive transducers," *IEEE Transactions on Magnetics*, 36(2), pp. 429-439, 2000.

[2] M.J. Dapino, R.C. Smith and A.B. Flatau, "A structural strain model for magnetostrictive transducers," *IEEE Transactions on Magnetics*, 36(3), pp. 545-556, 2000.

[3] J.E. Massad, R.C. Smith and G.P. Carman, "A free energy model for thin-film shape memory alloys," *Proceedings of the SPIE, Smart Structures and Materials 2003*, San Diego, CA, Volume 5049, pp. 13-23, 2003.

[4] D.K. Lindner, *Introduction to Signals and Systems*, McGraw-Hill, New York, 1999.

[5] J. Nealis, *Model-Based Robust Control Designs for High Performance Magnetostrictive Transducers*, Ph.D Dissertation, North Carolina State University, Raleigh, NC, 2003.

[6] J. Nealis and R.C. Smith, "Partial inverse compensation techniques for linear control design in magnetostrictive transducers," *Proceedings of the SPIE, Smart Structures and Materials, 2001*, Vol. 4326, pp. 462-473, 2001.

[7] J. Nealis and R.C. Smith, "Model-based robust control design for magnetostrictive transducers operating in hysteretic and nonlinear regimes," CRSC Technical Report CRSC-TR03-25; *IEEE Transactions on Automatic Control*, submitted.

[8] R.C. Smith, C. Bouton and R. Zrostlik, "Partial and full inverse compensation for hysteresis in smart material systems," *Proceedings of the 2000 ACC*, Chicago, IL, June 28-30, pp 2750-2754, 2000.

[9] R.C. Smith, M.J. Dapino and S. Seelecke, "A free energy model for hysteresis in magnetostrictive transducers," *Journal of Applied Physics*, 93(1), pp. 458-466, 2003.

[10] R.C. Smith, S. Seelecke, M.J. Dapino and Z. Ounaies, "A unified model for hysteresis in ferroic materials," *Proceedings of the SPIE, Smart Structures and Materials 2003*, San Diego, CA, Volume 5049, pp. 88-99, 2003.

[11] R.C. Smith, S. Seelecke, Z. Ounaies and J. Smith, "A free energy model for hysteresis in ferroelectric materials," CRSC Technical Report CRSC-TR03-01; *Journal of Intelligent Material Systems and Structures*, to appear.

[12] G. Tao and P. V. Kokotović, *Adaptive Control of Systems with Actuator and Sensor Nonlinearities*, John Wiley and Sons, New Jersey, 1996.

[13] K. Zhou and J.C. Doyle, *Essentials of Robust Control*, Prentice Hall, New Jersey, 1998.